JOURNAL OF SPACECRAFT AND ROCKETS
Vol. 47, No. 1, January–February 2010

Transonic Aerodynamics of a Lifting Orion Crew Capsule from Ballistic Range Data

Jeffrey D. Brown* and David W. Bogdanoff†
Eloret Corporation, Moffett Field, California 94035
Leslie A. Yates‡
Aerospace Computing, Inc., Mountain View, California 94043
and
Gary T. Chapman§
Eloret Corporation, Sunnyvale, California 94086

DOI: 10.2514/1.37878

Estimated nonlinear aerodynamic coefficients, including pitch- and yaw-damping derivatives, were obtained for a lifting model of the Orion crew capsule from experiments in the Hypervelocity Free-Flight Aerodynamics facility at NASA Ames Research Center. Nominal Mach numbers for the tests ranged from 0.70 to 1.25. A 44.45 mm-diameter powder gun launched the models through the 22.86 m-long test section, where their positions and attitudes were recorded with shadowgraph cameras at 16 optical stations. Data for nonlifting capsules were also taken. For angles of attack far from trim, both the lifting and nonlifting configurations appear to be stable in pitch damping. The symmetric models at supersonic speeds and the lifting models near Mach 0.7 show significant instability in pitch damping close to trim. For the latter case at small sideslip angles, yaw damping is also unstable.

Nomenclature

C_C	=	swerve force coefficient (normal to drag and lift)
C_D	=	drag coefficient (along wind axis)
cg	=	center of gravity
C_L	=	lift coefficient (upward relative to wind axis)
C_m	=	pitching moment coefficient
C_{m_α}	=	partial derivative of C_m with respect to α
C_{m_q}	=	pitch-damping coefficient (abbreviated form)
C_{n_r}	=	yaw-damping coefficient
C_n	=	yawing moment coefficient
d	=	model maximum diameter, cm (principal length scale)
$d1$	=	diameter of magnesium (Mg) and tungsten (W) inserts in lifting models, cm
h	=	model maximum length, cm (heatshield to aftbody)
I_{xx}, I_{yy}, I_{zz}	=	moment of inertia about roll, pitch and yaw axis, respectively, g-cm^2
$l1$	=	distance from virtual apex of model to junction of conical section and aft $R2$, cm
$l2$	=	distance from virtual apex to axis of Mg and W inserts in lifting models, cm
M	=	Mach number
$M1$	=	designation for solid steel model, nonlifting ($d = 3.56$ cm)
$M2$	=	designation for steel model with Mg and W inserts, lifting ($d = 3.56$ cm)
$M3$	=	designation for steel model with Mg and W inserts, lifting ($d = 1.52$ cm)
m	=	mass, g
p	=	pressure, torr
$R1$	=	model forebody radius, cm
$R2$	=	model fore (or aft) shoulder radius, cm
Re_D	=	Reynolds number, based on diameter
S	=	distance from model axis to interface between Mg and W inserts for lifting models, cm
T	=	temperature, °K
t	=	time, s
V	=	velocity, m/s
x, y, z	=	axial (+ = >downrange), transverse (+ = >port), and vertical (+ = >up) position, m
x_{cg}, y_{cg}, z_{cg}	=	axial, transverse, and vertical component of cg position, from virtual apex, cm
x_{cg-b}	=	axial component of cg position, from center of model base (aftbody), cm
α	=	pitch angle, deg
β	=	sideslip angle, deg
σ	=	total angle of attack, deg [$\sigma = \arccos(\cos\alpha^* \sin\beta)$]
θ	=	model inclination to x-y plane, deg ($+\theta$ = >heatshield up)
ρ	=	density, kg/m^3
ψ	=	model inclination to x-z plane, deg ($+\psi$ = >heatshield to port)
∞	=	freestream value
0	=	initial value, or value at launch
trim	=	value at trim
ref	=	reference value
rms	=	root mean square value
nom	=	nominal value

Presented as Paper 1232 at the 46th AIAA Aerosciences Meeting and Exhibit, Reno, NV, 7–10 January 2008; received 3 April 2008; accepted for publication 23 September 2009.

*Senior Research Scientist, Reacting Flow Environments Branch, NASA Ames Research Center, Mail Stop 230-2.
†Senior Research Scientist, Reacting Flow Environments Branch, NASA Ames Research Center, Mail Stop 230-2. Associate Fellow AIAA.
‡Vice President, 465 Fairchild Drive, Suite 224. Senior Member AIAA.
§Senior Research Consultant, 465 South Mathilda Avenue, Suite 103. Fellow AIAA.

Introduction

THE aerodynamic stability characteristics of a spacecraft descending through a planetary atmosphere are critical to its guidance, control and, most importantly, safety. The static stability properties determine how a vehicle will tend to trim. The tendency for perturbations in attitude about trim to either dampen out or amplify is driven by dynamic stability. A vehicle that maintains its nominal trim attitude and trajectory could still experience uncontrolled oscillations, a potentially fatal situation if it were to occur at a critical stage

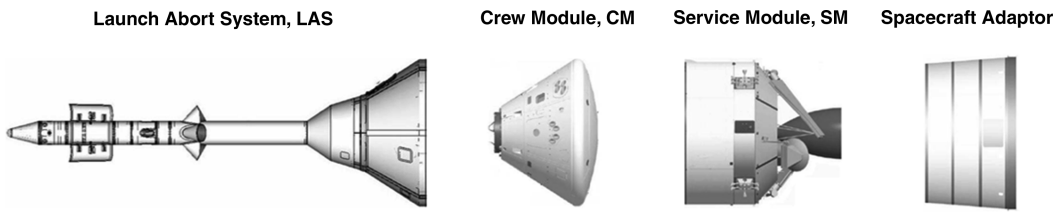

Fig. 1 CEV (Orion) components.

like parachute deployment. This was illustrated, almost tragically, during one of NASA's early Mercury flights, MA-6, when dynamic stability problems led to the expenditure of all of the capsule's reaction control system propellant and the oscillation amplitude grew to ± 20 deg before drogue chute deployment [1]. The current work was motivated by the need to mitigate such a risk for Orion, also called the crew exploration vehicle (CEV).

Orion will be the next NASA vehicle after Shuttle to support the human exploration of space. It consists of the four components illustrated in Fig. 1.

Figure 2 shows an early, simplified version of the crew module (CM) outer geometry upon which the current study is based. Except for the much larger scale, it is very similar to the Apollo capsule that flew NASA lunar missions four decades ago.

The dynamic stability of a vehicle, as will be discussed in the following section, is a function of both its static aerodynamic coefficients (such as of drag and lift) and its dynamic aerocoefficients (or derivatives), namely pitch and yaw damping. The latter are typically much harder to measure or predict than the former. An extensive experimental testing program was carried out in the 1960s to obtain aerodynamic stability data for the full range of configurations and atmospheric flight regimes relevant to the Apollo mission and abort trajectories [2]. Dynamic aerodata for the Apollo capsule were obtained both in aeroballistic ranges [3] and in wind tunnels [4].

The Apollo dynamic aerodata were used as initial entries in the CEV aerodatabase [5], but were not viewed as sufficient for guiding advanced designs of the CM. This is largely explained by the fact that, first, [1] cited the existence of significant problems in applying wind-tunnel dynamic aerodata to the six degree-of-freedom (DOF) motion of blunt lifting bodies, like the Apollo and CEV capsules. And, second, the critical techniques [6] and tools [7] now used to perform far more accurate nonlinear analyses on aeroballistic range data did not exist for Apollo.

This paper presents aerodynamic data pertaining particularly to parachute deployment for the Orion CM. The data were obtained from experiments in the Hypervelocity Free-Flight Aerodynamics Facility (HFFAF) at the NASA Ames Research Center. Tests were performed with both lifting and nonlifting scale models of a simplified CEV capsule geometry. The principal focus of the study was on the pitch-damping characteristics of the capsules in the Mach number range from 0.7 to 1.25.

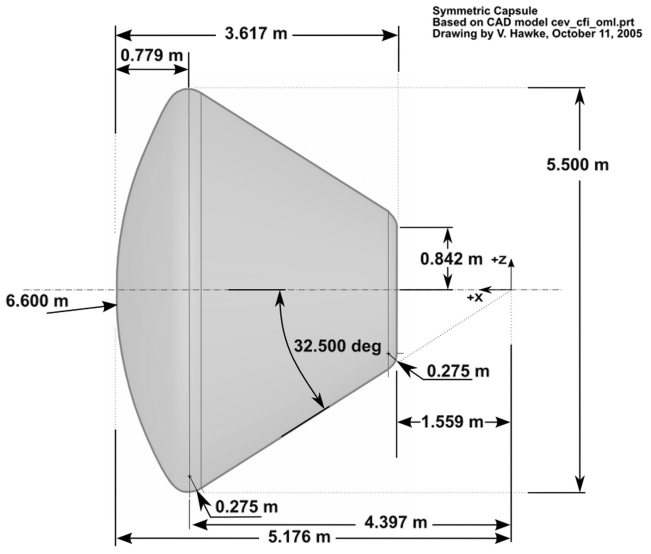

Fig. 2 Early, simplified CM outer geometry.

Experimental Facility and Setup

The HFFAF, shown schematically in Fig. 3, has a long heritage of supporting space exploration programs [8–11]. A 44.45 mm smooth-bore powder gun was used to launch the models. The 22.86 m-long test section, shown in Fig. 4, has 16 optical stations, spaced 1.52 m apart, where top and side view shadowgraph data were obtained.

As a test model flies past each optical station it penetrates a light sheet, which triggers high-intensity light emissions from two spark sources, one on top of the test section and one on the side. Each high-intensity beam is reflected and collimated by a spherical mirror and passed through the test section, forming a silhouette or shadow image of the flying projectile. The image is refocused on the opposite side through a high-speed (30–40 ns) Kerr cell electrooptical shutter, which freezes the model motion to the order of $0.0003 \cdot d$. The image is then expanded onto a 20×25 cm film plane to create a shadowgraph. High-speed counters record the precise time each shadowgraph is taken.

The test model is loaded into the gun breech inside a hard plastic cylindrical carrier, or sabot, which is cut into four lengthwise fingers. When the gun is fired and the launch package exits the muzzle,

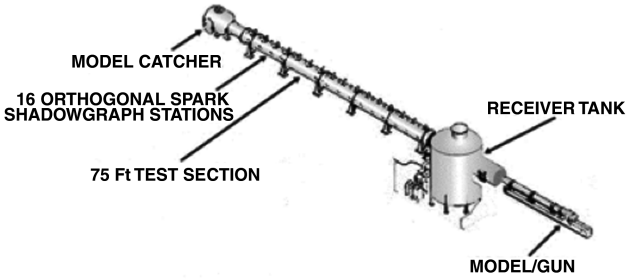

Fig. 3 Schematic of HFFAF aeroballistic range.

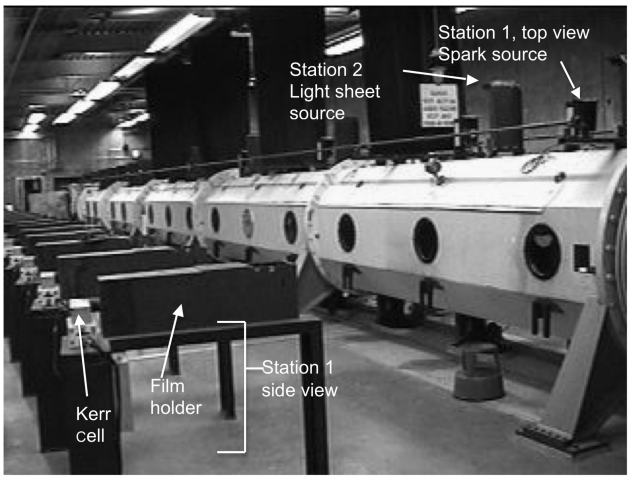

Fig. 4 HFFAF test section, port side.

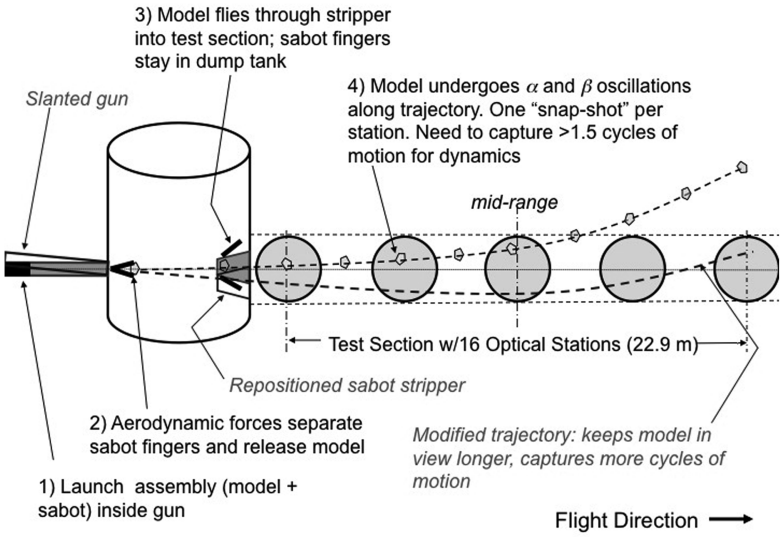

Fig. 5 Test shot sequence and effect of slanting gun.

aerodynamic forces separate the sabot fingers from the model. A few meters downrange, the fingers strike the outside of the conical steel stripper, remaining in the receiver tank, while the model flies through the center into the test section. This sequence is illustrated in Fig. 5.

A technique of slanting the gun, developed during previous testing [12], is also illustrated in Fig. 5. The technique was needed in the current work to obtain dynamic aeromeasurements for the lifting models. Had those models simply been launched along the facility centerline, they would have flown out of view only part way through the test section, making it impossible to record enough oscillatory motion for pitch or yaw damping to be measured. With the gun tilted, the parabolic path of the model reaches its minimum elevation inside the test section rather than at the gun muzzle, keeping the model in view longer and for a greater number of cycles. By also lowering the pressure in the test section (a unique capability of the HFFAF among operational aeroballistic ranges), lift could be reduced enough to keep the model in view for all 16 optical stations.

Test Models

Three model configurations, two lifting and one nonlifting, were tested. All were scale versions of the vehicle geometry in Fig. 2, but with differing cg locations and design trim angles.

The design outer mold line (OML) for all three models is shown, with dimensions as variables, in Fig. 6. Nominal (design) values of the dimensions are given in Table 1. The tungsten and magnesium slug inserts were used in the lifting models (only) to shift the cg off the model axis. The slugs were pressed into opposite sides of the model before its final OML was machined. The $M3$ were simply 42.7% scale models of the $M2$. The $M1$ were made of solid steel with the design cg at $(x_{cg}, y_{cg}, z_{cg}) = (0.676 \cdot d, 0, 0)$ relative to the virtual apex. For the $M2$ and $M3$, the nominal cg was located at $(x_{cg}, y_{cg}, z_{cg}) = (0.676 \cdot d, 0, -0.048 \cdot d)$ from the apex. The Orion will be a lifting vehicle; the $M1$ data were obtained to compare with the lifting data and with results of a previous nonlifting test conducted in a different facility [13].

Sabots, Launch Angles, and Pitch Amplitudes

Figure 7 is a drawing of an $M1$ model in a sabot. The model cavity is tilted down 40 deg to the sabot axis, so the resulting pitch angle at launch will be close to 140 deg. (Note: here we use the CEV program's convention for angle of attack, where 180 deg indicates level flight with the heat shield forward.) Launching the model this way creates an initial oscillation amplitude of approximately ±40 deg for the $M1$, which has a pitch angle at trim of 180 deg. Sabots with cavity angles of 0, 14, 19, and 30 deg were also used for the $M1$ to allow measurement of the pitch-damping coefficient versus α over a broad range of oscillation amplitudes. For $M = 0.7$, [5] showed the $M2$ models were expected to trim at $\alpha \approx 161$ deg, and sabot cavity angles of 14, 19, 19.7, 21.5, and 23.5 deg were used to launch them. The $M3$ models were predicted to have $\alpha_{trim} \approx 148$ deg at $M = 1.2$, and they were launched with sabot cavity angles of 27 and 32 deg.

The $M3$ models were designed for supersonic flight, where C_L was predicted to be much higher than for the $M2$s. This required a lower test pressure than for the $M2$s to keep the models in view for all

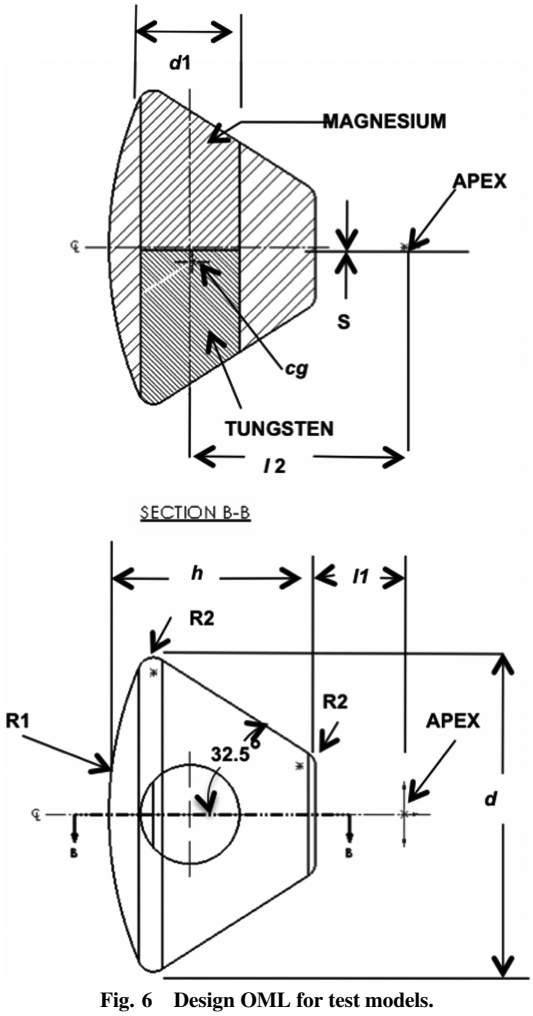

Fig. 6 Design OML for test models.

Table 1 Model dimensions, nominal

Model	d, cm	h, cm	$R1$, cm	$R2$, cm	$l1$, cm	$l2$, cm	$d1$, cm	S, cm
$M1$	3.557	2.338	4.267	0.178	1.008	N/A[a]	N/A[a]	N/A[a]
$M2$	3.557	2.338	4.267	0.178	1.008	2.430	1.118	0.038
$M3$	1.518	0.998	1.822	0.076	0.431	1.037	0.477	0.016

[a]not applicable

16 stations. However, lowering the pressure increases the oscillation wavelength, so the scale of the $M3$ models ($d_{\text{nom}} = 1.52$ cm) needed to be smaller than for the $M2$s to maintain an adequate number of cycles. The outer dimensions of the sabots, however, were determined by the size of the gun barrel, which remained the same throughout the test. Therefore, relative to the $M3$ models, the sabots were much larger and heavier than to the $M1$ and $M2$, and imparted a disproportionately strong kick to the $M3$ upon release, giving them a propensity to tumble in flight. This limited the amount of supersonic lifting-model data obtained.

It was initially difficult to generate small-amplitude oscillations about trim with the $M2$ models. In an attempt to smooth out the sabot separation process, a cylindrical cavity, 2.5 cm in diameter with a hemispherical end, was machined into the base (aft end) of each sabot, so that as the launch package (model + sabot) left the gun barrel, the blast of trailing, high-pressure muzzle gas helped to separate the sabot fingers. This technique was used very successfully during previous tests supporting the Space Shuttle return to flight effort [14], and it solved the current problem.

All sabots were made of Duraform, a nylon-based proprietary material, through selective laser sintering (SLS). Although SLS has significantly larger tolerances than machining, the large cavity angles used to set the oscillation amplitudes made machining the sabots impractical. The serrations and cavity section of each sabot finger were hand finished to improve fit and facilitate smooth separation.

Data Reduction and Analysis

Figure 8 shows side- and top-view shadowgraphs, taken simultaneously, of a capsule flying in the HFFAF. Such data were recorded at the 16 optical stations for each test shot. The air pressure and temperature in the test section were also recorded.

The shadowgraphs were digitized and reduced to trajectory data using the Comprehensive Aerodynamic Data Reduction System for Aeroballistic Ranges-1 (CADRA1) image processing and trajectory measurement program detailed in [7]. CADRA1 is an extension of the public domain application NIH Image, from the National Institutes of Health. Its extended features include object (e.g., model and fiducial wires) identification, two methods (least-squares and centroid) for measuring object position and orientation with subpixel resolution, and trajectory identification.

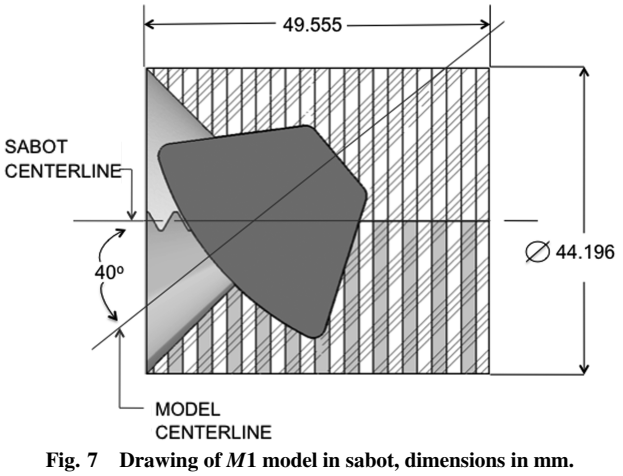

Fig. 7 Drawing of $M1$ model in sabot, dimensions in mm.

The positions and orientations of the model and fiducial wires (the latter are attached to the facility) were measured in each shadowgraph with CADRA1. Then, using a facility reference file, which contains the known locations of the fiducial wires in the facility, the image measurements were transformed to three-dimensional position and orientation measurements. These trajectory measurements provided the information necessary to identify the aerodynamic coefficients.

As a model flies down the range, the drag force slows it down, the lateral forces cause it to lift and swerve, the moments cause it to oscillate in pitch and yaw, and the pitch- and yaw-damping characteristics largely determine whether, with time, those oscillations grow or diminish in amplitude. For trimmed models, the rate at which the model slows down or swerves can be obtained from data at a few adjacent stations, and the frequency of a pitch or yaw oscillation can be determined if a little more than a half-cycle of the motion is captured. Therefore, data from only a few sequential optical stations may be sufficient to identify the static coefficients of force and moment, such as C_D, C_L, and C_m. However, to obtain the vehicle dynamics, for example, C_{m_q} and C_{n_r}, enough information must be available to measure the trim angle and the change in oscillation amplitude. For this, generally, 1.5–2 cycles of motion, with six to seven measurements per cycle, are required.

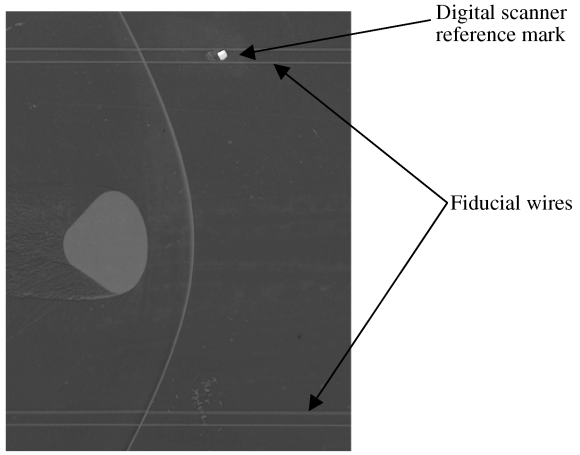

a)

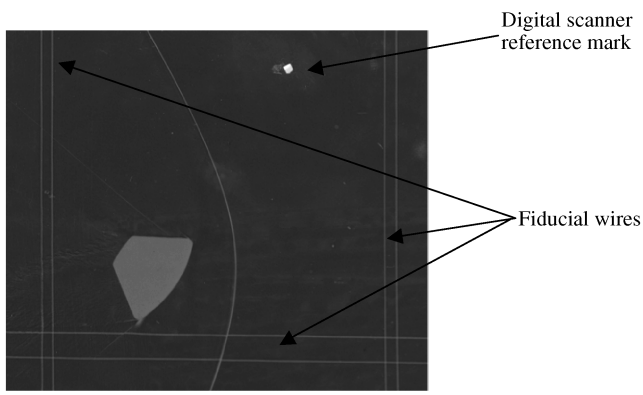

b)

Fig. 8 Shadowgraphs of flying capsule model: a) top view, b) side view.

Table 2 Model geometry and mass properties, measured

Model	Shot	d, cm	h, cm	m, g	x_{cg-b}, cm	y_{cg}, cm	z_{cg}, cm	I_{xx}, g-cm^2	I_{yy}, g-cm^2	I_{zz}, g-cm^2
$M1$	2366	3.556	2.342	96.615	1.387	0.000	0.000	104.534	86.257	86.257
$M1$	2379	3.556	2.339	96.300	1.387	0.000	0.000	103.679	80.549	80.549
$M1$	2380	3.556	2.344	97.013	1.387	0.000	0.000	105.076	81.715	81.715
$M1$	2384	3.556	2.342	96.563	1.389	0.000	0.000	104.208	81.024	81.024
$M1$	2386	3.559	2.339	96.484	1.392	0.000	0.000	104.398	81.051	81.051
$M1$	2388	3.553	2.342	96.324	1.392	0.000	0.000	103.951	80.658	80.658
$M1$	2393	3.553	2.339	96.424	1.387	0.000	0.000	104.127	80.685	80.685
$M1$	2439	3.553	2.342	96.350	1.392	0.000	0.000	103.842	81.254	81.254
$M1$	2365	3.556	2.339	96.475	1.389	0.000	0.000	105.564	84.901	84.901
$M1$	2378	3.561	2.342	97.336	1.387	0.000	0.000	105.225	81.946	81.946
$M1$	2437	3.553	2.339	96.187	1.397	0.000	0.000	103.720	80.441	80.441
$M1$	2438	3.546	2.334	95.476	1.387	0.000	0.000	102.120	80.210	80.210
$M2$	2425	3.559	2.337	101.067	1.389	0.000	−0.173	106.850	83.654	82.135
$M2$	2426	3.556	2.337	101.072	1.392	0.000	−0.173	107.340	83.383	81.593
$M2$	2427	3.556	2.332	102.064	1.384	0.000	−0.173	106.418	85.972	81.715
$M2$	2428	3.556	2.342	100.744	1.394	0.000	−0.168	107.625	83.600	81.905
$M2$	2429	3.556	2.337	101.020	1.389	0.000	−0.173	106.852	83.709	82.135
$M2$	2431	3.556	2.327	102.622	1.379	0.000	−0.170	106.039	83.898	82.298
$M2$	2433	3.556	2.342	101.378	1.392	0.000	−0.170	106.784	84.129	82.325
$M2$	2412	3.553	2.339	101.726	1.389	0.000	−0.170	105.889	80.129	82.420
$M2$	2413	3.553	2.334	101.427	1.397	0.000	−0.170	105.089	80.481	81.539
$M2$	2421	3.556	2.337	101.869	1.389	0.000	−0.170	107.340	83.274	81.824
$M3$	2397	1.519	1.003	7.747	0.599	0.000	−0.074	1.498	1.154	1.181
$M3$	2398	1.524	1.006	7.767	0.607	0.000	−0.074	1.543	1.163	1.167

The trajectory measurements obtained with CADRA1 were reduced to aerodynamic coefficients using the CADRA2 program, as described in [7]. In CADRA2, the coefficients are determined using a least-squares, differential correction procedure, which adjusts the aerodynamic parameters and initial conditions until a best least-squares fit of the trajectory measurements is obtained.

The aerodynamic coefficients were obtained from the trajectory measurements in three steps. First, individual shots were analyzed (single fits) using linear models for the aerodynamic coefficients. Generally, the variations in amplitude and Mach number for an individual test shot in the HFFAF are small, and nonlinear aerodynamics are not used when analyzing individual runs. The result of these single fits is, therefore, a set of quasi-linear, averaged coefficients that provide the best fits to the trajectories, or segments of trajectories, that are driven by nonlinear aerodynamics. By plotting the quasi-linear results, for example, average C_{m_q}, versus the rms value of any trajectory parameter, say α_{rms}, one can establish the existence of nonlinear trends in the coefficient's dependence on that parameter. For example, if there is no nonlinearity with α, the quasi-linear data plotted versus α_{rms} will fall on a straight line. However, if there are nonlinearities, the plotted quasi-linear data will define a curve.

The shapes of the curves plotted in step 1 provided information for the second step of the process, selecting the functional forms with which to represent the nonlinear aerodynamics. Although it is not possible to extract the actual nonlinear aerodynamic-coefficient equations from the quasi-linear plots, it is possible to identify the general functions that will adequately capture the nonlinearities.

Table 3 Shot flight and launch parameters

Model	Shot	M_∞	Re_∞	V_∞, m/s	P_∞, torr	T_∞, °K	ρ_∞, kg/m^3	α_0, deg	α_{trim}, deg
$M1$	2366	1.07	8.66×10^5	370.3	761.2	297.2	1.190	140.0	180.0
$M1$	2379	1.06	8.55×10^5	364.9	759.2	295.8	1.192	140.0	180.0
$M1$	2380	1.10	8.89×10^5	380.1	759.2	296.2	1.191	140.0	180.0
$M1$	2384	1.08	8.71×10^5	372.5	760.5	296.7	1.191	180.0	180.0
$M1$	2386	1.11	8.95×10^5	382.8	758.2	296.2	1.189	180.0	180.0
$M1$	2388	1.07	8.70×10^5	370.9	762.8	296.7	1.194	150.0	180.0
$M1$	2393	1.13	9.15×10^5	389.8	762.0	296.0	1.196	150.0	180.0
$M1$	2439	1.24	10.2×10^5	427.6	768.6	294.3	1.213	166.0	180.0
$M1$	2365	1.39	11.2×10^5	480.1	760.0	297.1	1.188	140.0	180.0
$M1$	2378	1.25	10.1×10^5	431.0	760.0	297.2	1.188	140.0	180.0
$M1$	2437	1.25	10.2×10^5	430.9	764.1	294.6	1.205	161.0	180.0
$M1$	2438	1.27	10.3×10^5	436.7	762.0	294.1	1.204	180.0	180.0
$M2$	2425	0.58	2.10×10^5	199.1	340.0	294.8	0.536	161.0	159.4
$M2$	2426	0.64	2.31×10^5	219.4	340.0	294.9	0.536	161.0	159.1
$M2$	2427	0.67	2.42×10^5	229.7	339.9	294.7	0.536	166.0	158.9
$M2$	2428	0.66	2.39×10^5	226.6	340.0	294.5	0.536	158.5	158.9
$M2$	2429	0.69	2.49×10^5	236.3	340.1	294.7	0.536	160.3	158.7
$M2$	2431	0.73	2.66×10^5	252.1	340.0	293.9	0.538	156.5	158.5
$M2$	2433	0.66	2.83×10^5	227.0	400.0	293.3	0.634	156.5	158.9
$M2$	2412	0.91	3.30×10^5	314.5	339.8	295.1	0.535	166.0	154.7
$M2$	2413	0.95	3.44×10^5	326.5	340.7	294.9	0.537	166.0	152.3
$M2$	2421	0.90	3.27×10^5	310.7	340.1	294.9	0.536	161.0	155.4
$M3$	2397	1.29	0.48×10^5	445.3	82.3	295.0	0.130	154.0	145.0
$M3$	2398	1.13	0.43×10^5	390.1	83.4	295.5	0.131	154.0	147.1

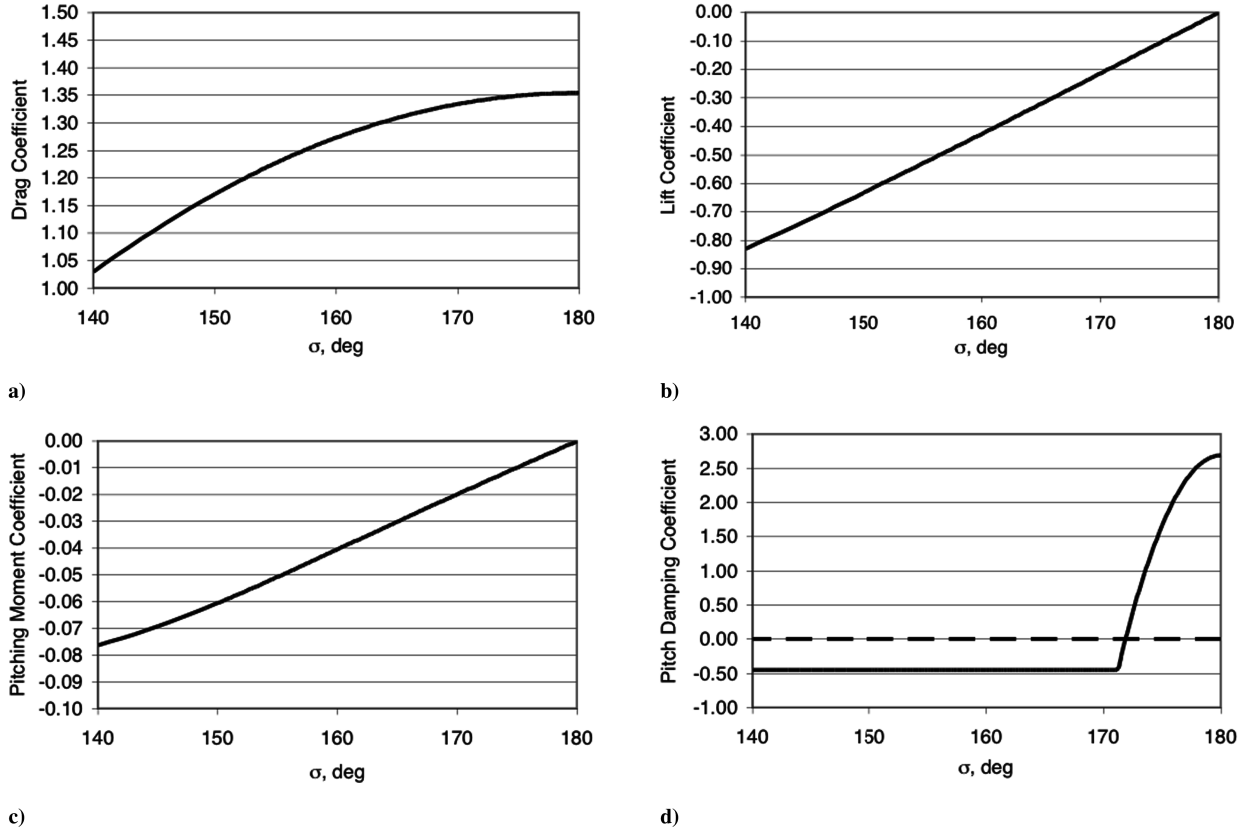

Fig. 9 Aerocoefficients for $M1$ model at $M_{\text{nom}} = 1.10$: a) C_D, b) C_L, c) C_m, and d) C_{m_q}.

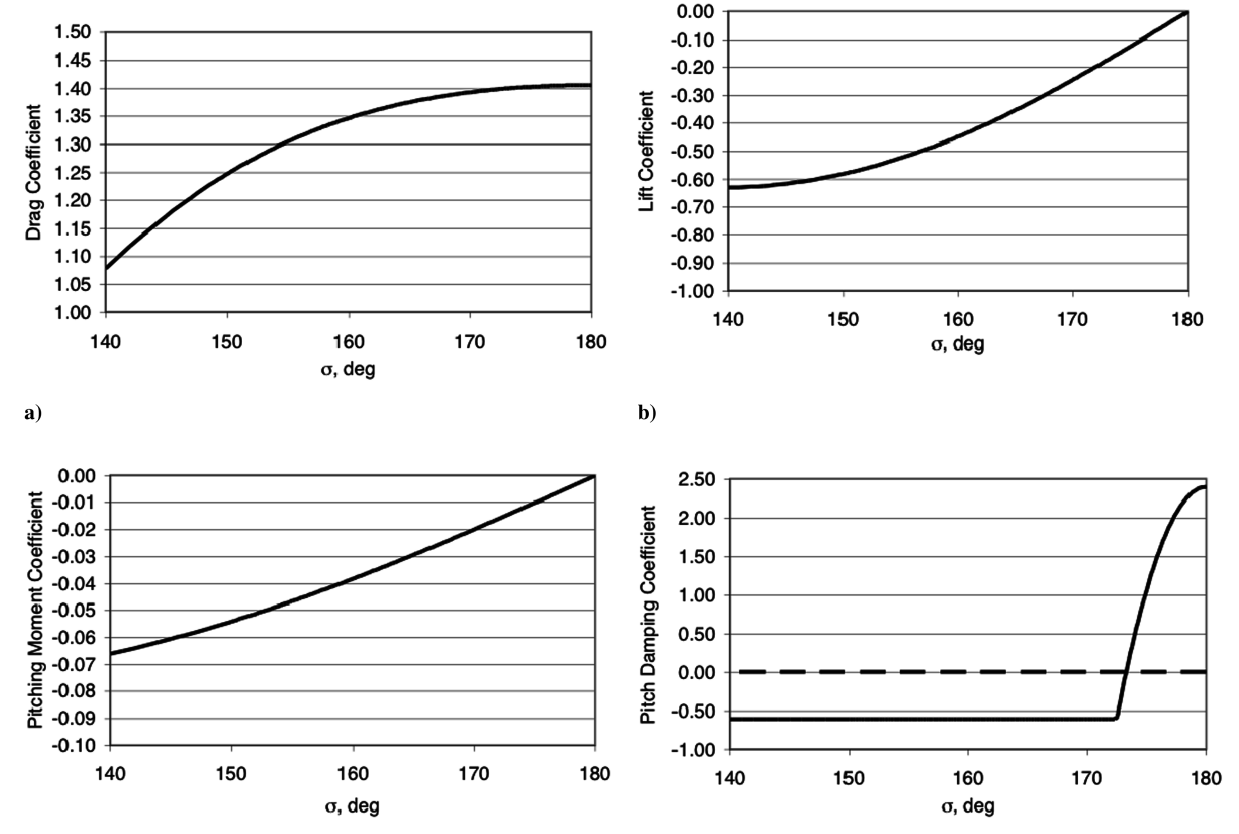

Fig. 10 Aerocoefficients for $M1$ model at $M_{\text{nom}} = 1.25$: a) C_D, b) C_L, c) C_m, and d) C_{m_q}.

With the general modeling functions selected, shots of projectiles with similar cg locations and flying at similar Mach numbers were analyzed simultaneously (multifits) to obtain the proper constant parameters within the functions and, therefore, the full expressions for the nonlinear aerodynamic coefficients. During the test, for each combination of M and cg, shots with a wide range of oscillation amplitudes were made. By including data over a broad spectrum of α_{rms} in the multifits, the accuracies of the resulting aerodynamic coefficients were improved.

Results

Authors' note: the angle conventions used by CADRA are those from classical aerodynamics ([15]), where zero pitch and zero yaw angle (or zero total angle of attack, for nonlifting models) implies direct, heatshield-forward flight. Under the standard CEV convention, however, the same type of flight is denoted by 180 deg of pitch and zero yaw (or, for nonlifting models, total angle of attack equals 180 deg). In this paper, both conventions were used in order to avoid the introduction of any systematic conversion errors; the convention used in a particular table or figure is either noted in the heading/caption or is apparent from the values tabulated or plotted.

Tables 2 and 3 provide the measured model properties and flight parameters, respectively, for the test shots used in this investigation to obtain aerodynamic coefficients. The values given for velocity, Mach number, Reynolds number and trim angle are effectively averages, measured midway along the test section. A nominal viscosity for air, at 295 K, was used to compute Re_D.

Figure 9 and 10 show plots of C_D, C_L, C_m, and C_{m_q} versus total angle of attack, σ, for the $M1$ model at $M_{\text{nom}} = 1.10$ and $M_{\text{nom}} = 1.25$, respectively. Total angle of attack is used as the independent variable, because α and β are indistinguishable for symmetric models.

All of the functions are symmetric about $\sigma = 180$ deg. The results show that for a symmetric, nonlifting capsule, pitch damping stabilizes the motion (for blunt bodies, this typically means $C_{m_q} < 0$) at large angles away from trim (i.e., $\sigma = 180$ deg) but is significantly destabilizing, with large positive values close to trim. The destabilizing effect peaks at $\sigma = 180$ deg and extends more than 5 deg to either side.

This behavior of C_{m_q} is suggested for the symmetric case by the three trajectory angle plots, for $M1$ models at $M_{\text{nom}} = 1.10$, shown in Fig. 11. In Fig. 11a, the model shows a large-amplitude pitch oscillation, which, although not damped, appears to be stable with time. The motion in Fig. 11b, with medium amplitude, is seen to be getting slightly larger. The model undergoing small-amplitude oscillations in Fig. 11c shows a clear dynamic instability, which is to say the oscillations are growing rapidly.

When simplifications afforded by short-duration, constant-altitude flight (as in an aeroballistic range) are applied to the general criterion for dynamic stability derived by Sommer and Tobak [16] for the oscillatory motion of an Earth-entry vehicle, the resulting expression for dynamic stability of the test models undergoing planar (e.g., pitching) motion in the HFFAF becomes

$$C_D - C_{L_\alpha} + C_{m_q}\left(\frac{md^2}{I_{yy}}\right) < 0 \tag{1}$$

where C_{L_α} is the slope of the lift-coefficient curve, versus alpha. For the $M1$ models, the quantity (md^2/I_{yy}) approximately equals 15. For the three trajectories shown in Fig. 11, the value of $C_D - C_{L_\alpha}$ is roughly the same: about 2.6. Therefore, to stabilize the oscillatory motion, Eq. (1) implies that C_{m_q} must be less than approximately -0.17. This agrees with the general rule of thumb for blunt bodies, that $C_{m_q} < 0$ has a stabilizing effect, and $C_{m_q} > 0$ is destabilizing. It also means that the trajectories plotted in Fig. 11 substantiate the form of C_{m_q} given in Fig. 9d.

Figure 12 shows the aerodynamics for the $M2$ model at $M_{\text{nom}} = 0.70$. Results are provided for the yaw plane as well as the pitch plane. However, because the former data were all obtained for

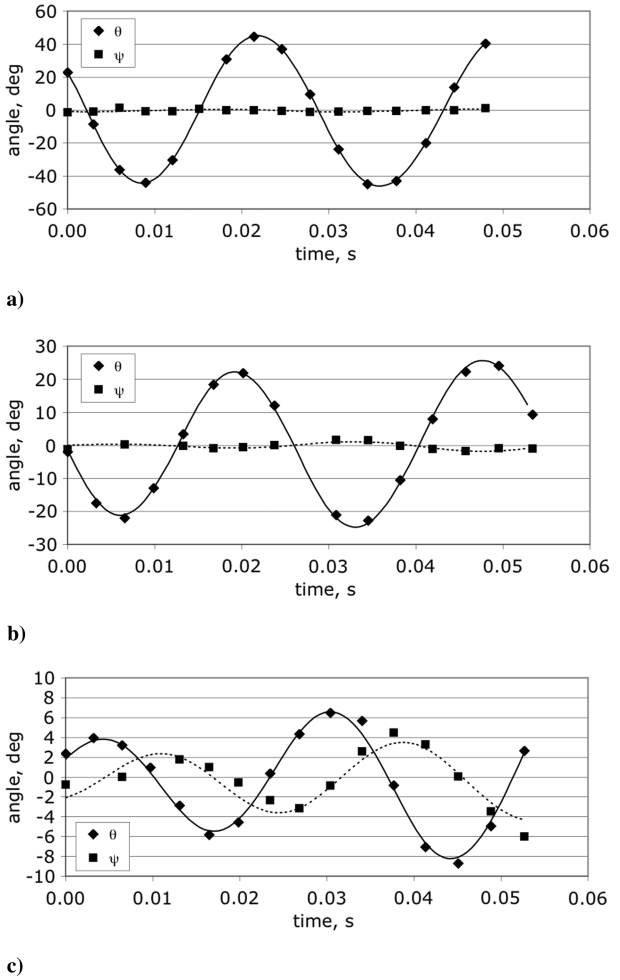

Fig. 11 Trajectory angles, $M1$ model, $M_{\text{nom}} = 1.10$: a) large α_{rms}, b) medium α_{rms}, and c) small α_{rms}.

cases where β was small and either of the same order as or much smaller than α, they should be taken to be independent of α and valid for small β only.

There is a small increase in C_D with Mach number in this speed range, which becomes more pronounced as α moves farther from 180 deg. A very small M effect is also seen in the pitching moment coefficient. As with the small-amplitude behavior of C_{m_q} for the $M1$ models, yaw damping C_{n_r} is positive, that is, unstable, for small β.

The $M2$ model appears to be very stable in pitch damping for $M_{\text{nom}} = 0.70$, except at very small angles about the nominal trim, $\alpha = 159$ deg. The nonlinear function that describes the behavior of C_{m_q} with α was obtained by simultaneously fitting trajectories from shots having a range of pitch-oscillation amplitudes. The average C_{m_q} values obtained from linear aerodynamics and used to choose the nonlinear function for the multifit data, per steps one and two of the three-step process described in the Sabots, Launch Angles, and Pitch Amplitudes section, are represented in Fig. 12d, for large and small amplitudes, by the lower and upper dashed lines, respectively.

Figure 13 and 14 show the pitch-plane aerodynamics for lifting capsules at $M_{\text{nom}} = 0.93$ and $M_{\text{nom}} = 1.20$, respectively. As with the lifting $M_{\text{nom}} = 0.70$ case, a Mach number effect is seen in C_D and C_m. Only two or three trajectories were obtained in each case, which made it difficult to choose the functional forms to model the nonlinear portion of C_m. Therefore, CFD results from [5] were used to guide the selection. The resulting 6 DOF fits of the measured trajectory data were very good, which bolsters confidence in the CFD.

For $M_{\text{nom}} = 0.93$ and $M_{\text{nom}} = 1.20$, no trajectories were recorded with small enough amplitude to determine C_{m_q} close to trim: approximately $\alpha = 153.5$ deg and $\alpha = 146.5$ deg, respectively.

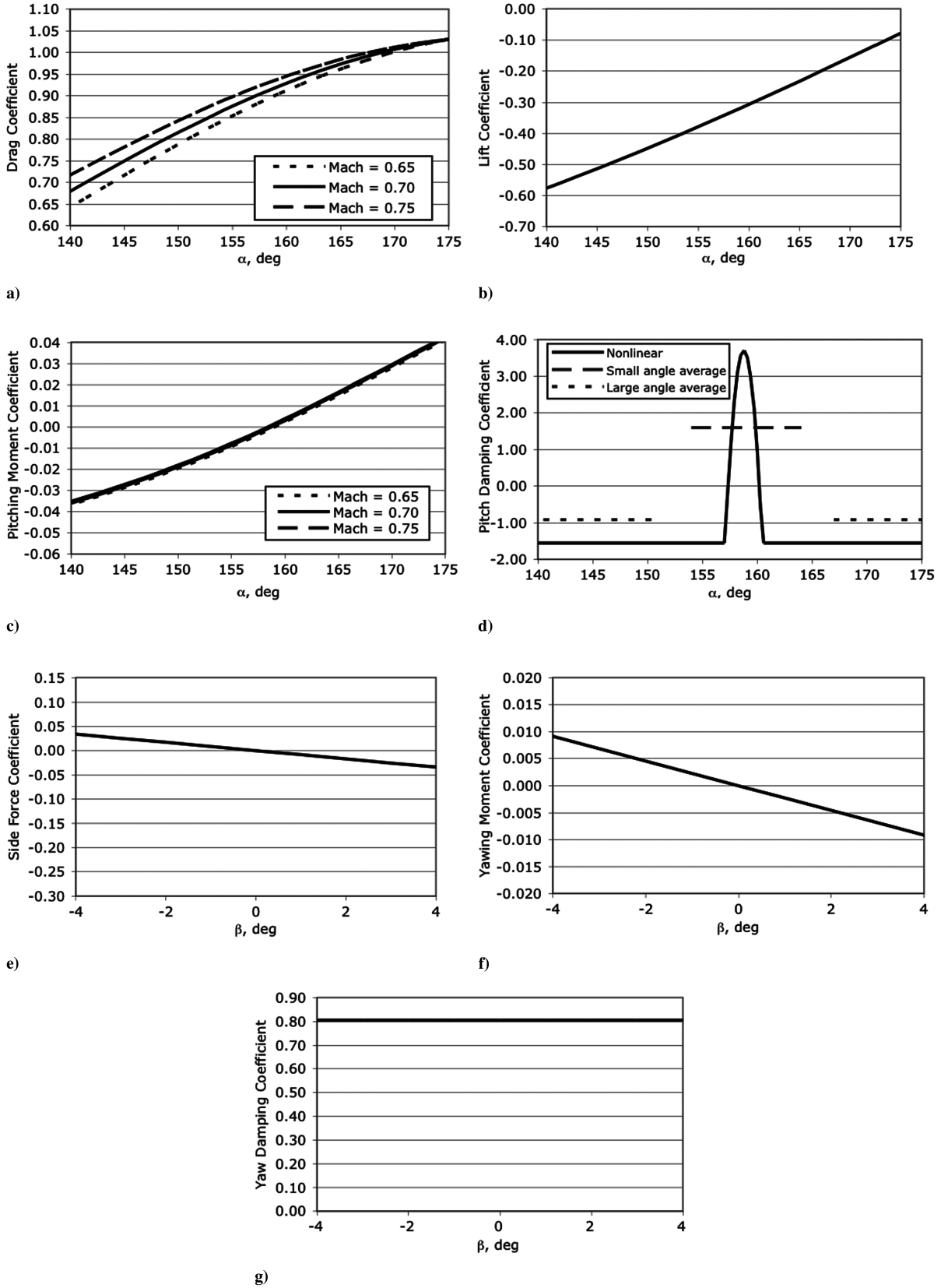

Fig. 12 Aerocoefficients for $M2$ model at $M_{\text{nom}} = 0.70$: a) C_D, b) C_L, c) C_m, d) C_{m_q}, e) C_C, f) C_n, and g) C_{n_r}.

Consequently, the pitch-damping curves in Figs. 13 and 14 have gaps in the neighborhood of trim. At large angles, C_{m_q} is stabilizing for both Mach numbers.

Table 4 provides the equations and constant parameters that describe the estimated nonlinear aerodynamics plotted in Figs. 9, 10, and 12–14. They were determined in CADRA2 to provide the best 6-DOF fits to the measured trajectory data. Where no value is shown for a parameter that appears in the functional form of an aerocoefficient, the term modified by that parameter in the equation was not used to fit the data.

Table 4 seems to show a yaw, or sideslip angle dependency in the expressions for C_D and C_L of the lifting capsules, however, no such

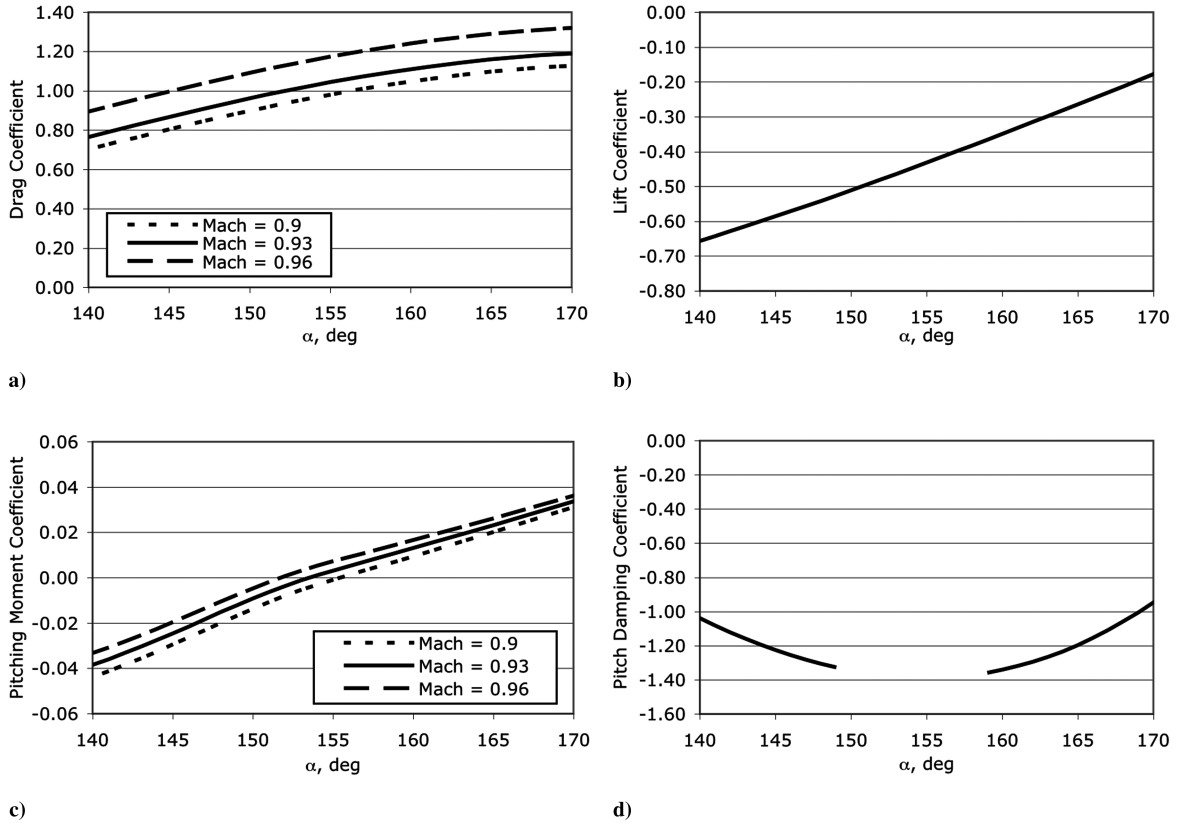

Fig. 13 Aerocoefficients for $M2$ model at $M_{\text{nom}} = 0.93$: a) C_D, b) C_L, c) C_m, and d) C_{m_q}.

relation is reflected in the associated plots of Figs. 12–14. This is because the yaw angle only appears in the equations as $\cos\beta$ or $\cos^2\beta$, both of which are approximately one for the small β values considered.

Uncertainties

There are two primary sources of uncertainties in the estimated aerodynamic coefficients obtained in this investigation. The first is experimental errors. These include errors in the measured

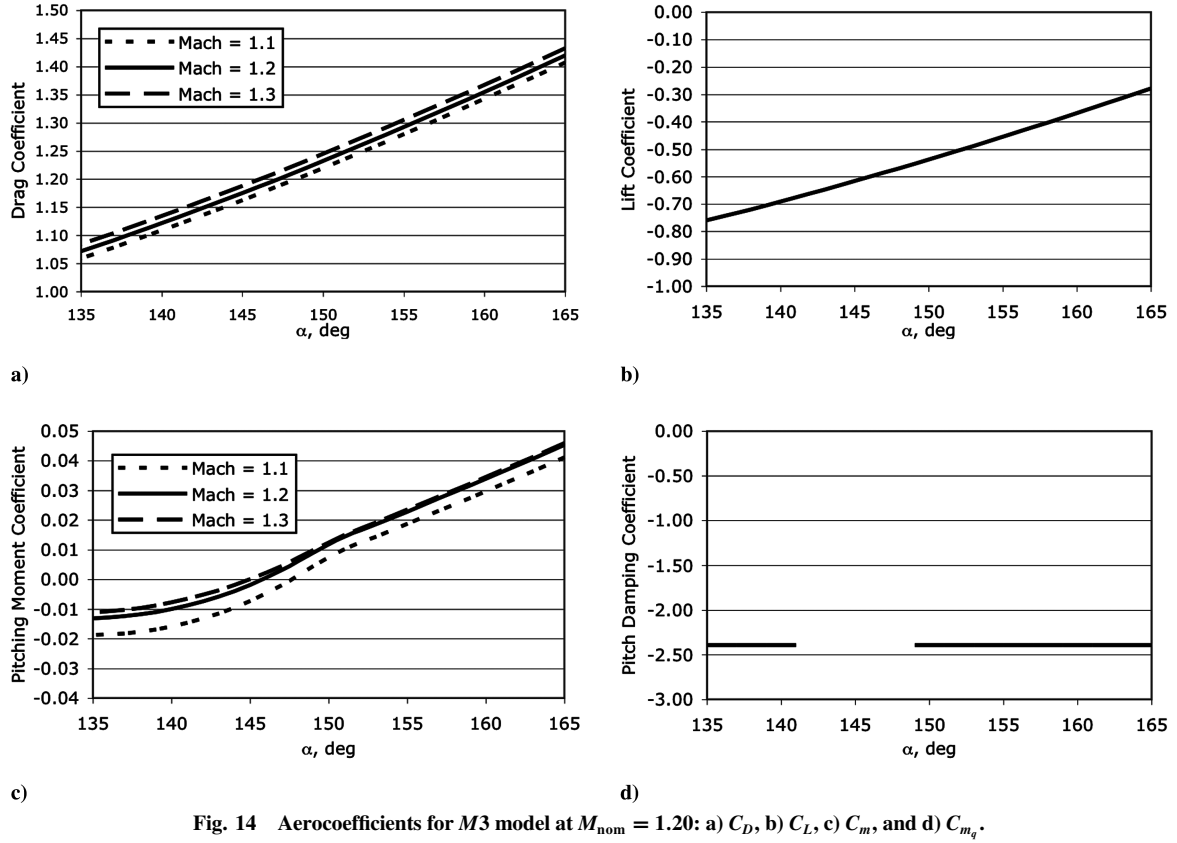

Fig. 14 Aerocoefficients for $M3$ model at $M_{\text{nom}} = 1.20$: a) C_D, b) C_L, c) C_m, and d) C_{m_q}.

Table 4 Equations and constant parameters for estimated aerodynamic coefficients (angle convention from classical aerodynamics)

Case	Aerocoefficient	Functional form	A_1	A_2	A_3	A_4	A_5	A_6	a_{ref}, deg
*M*1 *M*1.10	C_D	$A_1 + A_2(M_\infty - M_{\text{ref}}) + A_3(M_\infty - M_{\text{ref}})^2 + [A_4 + A_5(M_\infty - M_{\text{ref}})]\sin^2\sigma + A_6\sin^4\sigma$	1.361	0.516	−2.784	−0.723	−0.467	−0.191	0.00
“	C_L	$[A_1 + A_2(M_\infty - M_{\text{ref}}) + A_3(M_\infty - M_{\text{ref}})^2 + A_4\sin^2\sigma + A_5\sin^4\sigma]\sin\sigma$	−1.470	−0.082		0.461			
“	C_m	$[A_1 + A_2(M_\infty - M_{\text{ref}}) + A_3\sin^2\sigma + A_4\sin^4\sigma]\sin\sigma$	−0.1170	0.0273	−0.0176	0.0402			
“	C_{m_q}	$\max(A_1, A_2 + A_3\sin^2\sigma)$	−0.967	3.900	−174.24				
*M*1 *M*1.25	C_D	$A_1 + A_2(M_\infty - M_{\text{ref}}) + A_3(M_\infty - M_{\text{ref}})^2 + [A_4 + A_5(M_\infty - M_{\text{ref}})]\sin^2\sigma + A_6\sin^4\sigma$	1.406	0.226	−1.252	−0.392	0.105	−0.968	
“	C_L	$[A_1 + A_2(M_\infty - M_{\text{ref}}) + A_3(M_\infty - M_{\text{ref}})^2 + A_4\sin^2\sigma + A_5\sin^4\sigma]\sin\sigma$	−1.328	−0.740		1.111			
“	C_m	$[A_1 + A_2(M_\infty - M_{\text{ref}}) + A_3\sin^2\sigma + A_4\sin^4\sigma]\sin\sigma$	−0.1151	0.0010	0.0262	0.0096			
“	C_{m_q}	$\max(A_1, A_2 + A_3\sin^2\sigma)$	−0.604	2.400	−174.24				
*M*1 *M*0.70	C_D	$A_1 + A_2(M_\infty - M_{\text{ref}}) + A_3(M_\infty - M_{\text{ref}})^2 + [A_4 + A_5(M_\infty - M_{\text{ref}})](\sin\alpha - \sin\alpha_{\text{ref}})\cos\beta + A_6(\sin\alpha - \sin\alpha_{\text{ref}})^2\cos^2\beta$	0.953	0.276		−0.531	1.357	−0.774	21.21
“	C_L	$[A_1 + A_2(\sin\alpha - \sin\alpha_{\text{ref}})\cos\beta + A_3(\sin\alpha - \sin\alpha_{\text{ref}})^2\cos^2\beta + A_4(M_\infty - M_{\text{ref}})]\sin\alpha\cos\beta$	−0.896						
“	C_m	$\alpha < \alpha_{\text{ref}}$: $A_2 + A_3(M_\infty - M_{\text{ref}}) + A_1(\sin\alpha - \sin\alpha_{\text{ref}})$ $\alpha > \alpha_{\text{ref}}$: $A_2 + A_3(M_\infty - M_{\text{ref}}) + A_1(\sin\alpha - \sin\alpha_{\text{ref}}) + A_4(\sin\alpha - \sin\alpha_{\text{ref}})^2$	−0.1532	0.0095	0.0150	0.0614			
“	C_{m_q}	$\max[A_1, A_2 + A_3(\sin\alpha - \sin\alpha_{\text{ref}})^2]$	−1.553	3.700	−6895				
“	C_C	$A_1\sin\beta$	−0.486						
“	C_n	$A_1\sin\beta$	−0.1316						
“	C_{n_r}	A_1	0.810						
*M*2 *M*0.93	C_D	$A_1 + A_2(M_\infty - M_{\text{ref}}) + A_3(M_\infty - M_{\text{ref}})^2 + [A_4 + A_5(M_\infty - M_{\text{ref}})](\sin\alpha - \sin\alpha_{\text{ref}})\cos\beta + A_6(\sin\alpha - \sin\alpha_{\text{ref}})^2\cos^2\beta$	0.981	1.006	36.930	−0.950		−1.448	25.87
“	C_L	$[A_1 + A_2(\sin\alpha - \sin\alpha_{\text{ref}})\cos\beta + A_3(\sin\alpha - \sin\alpha_{\text{ref}})^2\cos^2\beta + A_4(M_\infty - M_{\text{ref}})]\sin\alpha\cos\beta$	−1.020						
“	C_m	$\alpha < \alpha_{\text{ref}}$: $A_2 + A_4(M_\infty - M_{\text{ref}}) + [A_1 + A_5(M_\infty - M_{\text{ref}})](\sin\alpha - \sin\alpha_{\text{ref}})$ $\alpha > \alpha_{\text{ref}}$: $A_2 + A_4(M_\infty - M_{\text{ref}}) + [A_1 + A_5(M_\infty - M_{\text{ref}})](\sin\alpha - \sin\alpha_{\text{ref}})$ $+A_3[0.0079 - 0.9495(\sin\alpha - \sin\alpha_{\text{ref}}) + 2.2388(\sin\alpha - \sin\alpha_{\text{ref}})^2](\sin\alpha - \sin\alpha_{\text{ref}})$	−0.1283	−0.0007	0.7275	0.1346	0.2040		
“	C_{m_q}	$A_2 + A_3(\sin\alpha - \sin\alpha_{\text{ref}})^2$		−1.390	7.140				
“	C_C	$A_1\sin\beta$	−0.291						
“	C_n	$A_1\sin\beta$	−0.1507						
“	C_{n_r}	A_1	0.590						
*M*3 *M*1.20	C_D	$A_1 + A_2(M_\infty - M_{\text{ref}}) + A_3(M_\infty - M_{\text{ref}})^2 + [A_4 + A_5(M_\infty - M_{\text{ref}})](\sin\alpha - \sin\alpha_{\text{ref}})\cos\beta + A_6(\sin\alpha - \sin\alpha_{\text{ref}})^2\cos^2\beta$	1.233	0.127		−0.777			33.99
“	C_L	$[A_1 + A_2(\sin\alpha - \sin\alpha_{\text{ref}})\cos\beta + A_3(\sin\alpha - \sin\alpha_{\text{ref}})^2\cos^2\beta + A_4(M_\infty - M_{\text{ref}})]\sin\alpha\cos\beta$	−1.073						
“	C_m	$\alpha < \alpha_{\text{ref}}$: $A_2 + [A_1 + A_5(M_\infty - M_{\text{ref}})](\sin\alpha - \sin\alpha_{\text{ref}}) + A_4[0.0252 - 0.044(M_\infty - M_{\text{ref}})](M_\infty - M_{\text{ref}})$ $\alpha > \alpha_{\text{ref}}$: $A_2 + [A_1 + A_5(M_\infty - M_{\text{ref}})](\sin\alpha - \sin\alpha_{\text{ref}}) + A_4[0.0252 - 0.044(M_\infty - M_{\text{ref}})](M_\infty - M_{\text{ref}})$ $+A_3\{[-0.1093 + 0.2665(M_\infty - M_{\text{ref}})] + [0.61 + 0.90(M_\infty - M_{\text{ref}})](\sin\alpha - \sin\alpha_{\text{ref}})\}(\sin\alpha - \sin\alpha_{\text{ref}})$	−0.1373	0.0124	0.8463	0.9563			
“	C_{m_q}	$A_2 + A_3(\sin\alpha - \sin\alpha_{\text{ref}})^2$	−2.390						

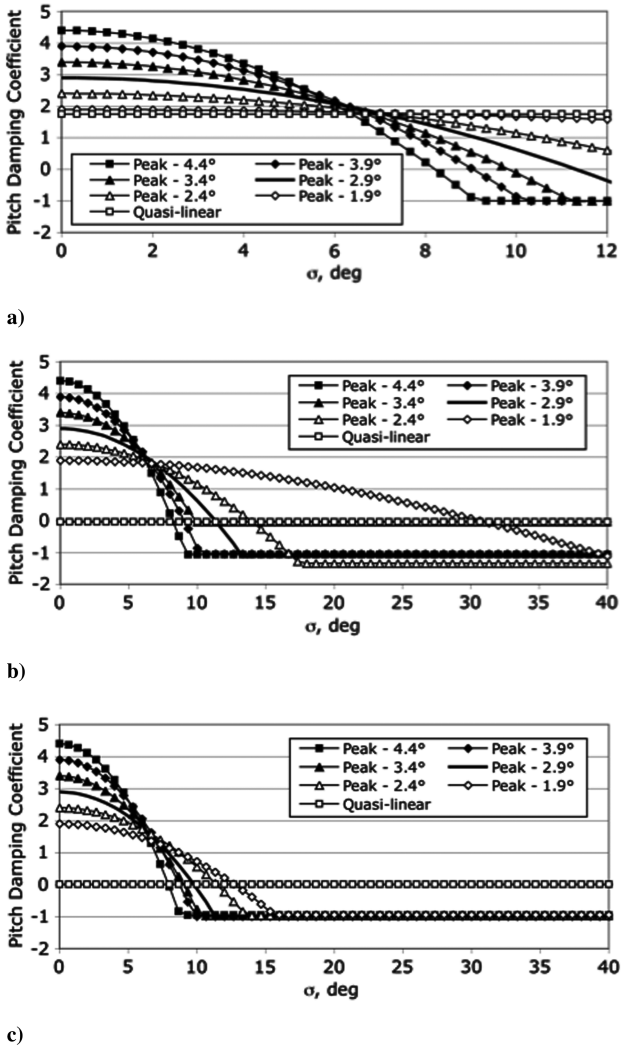

Fig. 15 C_{m_q} sensitivity to peak value: a) small-amplitude data only, b) fixed small-angle behavior, all data, and c) fall-off rate and asymptote allowed to vary, all data.

dimensions and inertial properties of the models, test conditions, times, and model positions and orientations. The errors in the position and orientation measurements result from optical distortions, film-reading errors, and uncertainties in the locations of the facility fiducial system. The latter can be minimized by 1) keeping a historical record of the differences at each optical station between the calculated and measured trajectory points, and 2) making calibration test shots with a projectile of simple and known aerodynamics. Both of these procedures help identify biases in the measured data. For this test series, calibration shots were made with spherical steel models. The differences between the calculated and measured trajectory points for the sphere shots were used to identify biases in the position measurements at each station. Measurement errors did not significantly affect the uncertainties in the estimated coefficients for this experiment.

The second and, for this work, most significant source of uncertainties is the selection of the analytic functions to model the aerodynamic coefficients. As discussed in the Data Reduction and Analysis section, functional forms with unknown constant parameters are assumed for the coefficients. The unknowns are then estimated by a differential least-squares technique that fits calculated trajectories to the measured trajectory points. Uncertainties are introduced into the parameter estimates when there are insufficient data to accurately differentiate between the effects of the various parameters. In addition, the functional forms are approximations and may contribute to uncertainties that cannot be identified unless sufficient experimental information is available.

As an example of the sensitivity of the nonlinear coefficients to mathematical modeling, we consider C_{m_q} for the $M1$ model at $M_{\text{nom}} = 1.10$. A linear fit of the quasi-linear or average C_{m_q} versus σ_{rms} was used to define the peak pitch-damping value at $\sigma = 0$ deg. Because there were only two shots where σ_{rms} was small, a relatively large uncertainty in the peak value of C_{m_q} was expected. To demonstrate the sensitivity of C_{m_q} to its peak value, several peak values were selected, and the rate at which C_{m_q} falls off with σ was identified within CADRA2, which allows the user to hold one parameter (e.g., peak height or large-angle asymptote) constant while examining how the others vary. Initially, to examine small-angle behavior, a constant lower limit of -1.0 was imposed on C_{m_q}. The results, shown in Fig. 15a, demonstrate the strong relationship between the peak C_{m_q} and the rate at which C_{m_q} falls off with total angle of attack. The best fit to the data was obtained with C_{m_q} a constant. However, this was rejected because a constant, positive C_{m_q} would have been unrealistic for the large-amplitude motions, which were not included in the analysis.

Despite the large variation in the pitch-damping coefficient exhibited in Fig. 15a, further examination provides some confidence in the pitch-damping math model and the resulting estimated C_{m_q}. For the case of the $M1$ model at $M_{\text{nom}} = 1.10$, σ_{rms} for the two small-amplitude trajectories is approximately 7 deg. In Fig. 15a, in the range of 6–7 deg, there is reasonably good agreement between all C_{m_q} curves regardless of the peak value. If the peak value estimate is too high or too low, the width of the peak becomes narrower or wider, respectively, and so the pitch-damping model will capture the proper growth rate for small angles, but not necessarily for very small ones.

To investigate the impact of uncertainties in small-angle pitch damping on large-angle behavior, the former was modeled using just the two small-angle data sets, and the large-angle asymptote was identified using all of the $M1$, $M_{\text{nom}} = 1.10$ trajectory data. The results are shown in Fig. 15b. For peak values ranging from 2.9 to 4.4, the asymptote is -1.06 ± 0.06; for a peak value of 2.4, the asymptote is more negative, -1.35; for 1.9, it is -5.47. For peak values ranging from 2.4 to 4.4, the rms difference between the calculated and experimental values of σ ranged from 0.76 to 0.81 deg. For a peak value of 1.9, the quality of the fits showed significant deterioration; the rms difference was 2.5 times greater than for the other cases. There again appears to be significant variation in the pitch damping, but the differences are driven by the small-angle behavior. The aerodynamic model with peak pitch-damping values ranging from 2.9 to 4.4 would provide good estimates of motions with large amplitudes.

In Fig. 15c, the pitch-damping coefficients are shown for several fixed peak values but with variable fall-off rates and asymptotes. For peak values from 1.9 to 4.4, the large-angle asymptote ranges from -0.94 to -1.0. The rms difference between the calculated and experimental values for σ ranged from 0.74 to 0.81 deg. Again, the fall-off rate at small angles compensates for errors in the peak value, so that the amplitude growth is captured at small, but not very small, angles. The pitch damping at large angles is largely independent of the pitch damping at 0 deg.

This sensitivity analysis of C_{m_q} for the $M1$ model at $M_{\text{nom}} = 1.10$ gives guidance on improving the accuracy of the estimated pitch damping in general. For the $M1$ case, more data in the 10–20 deg amplitude range are needed to differentiate between the various small-angle models and to further test the complete pitch-damping model. Additional data would also be useful in determining whether a dependency on angle of attack exists for the large-angle asymptote.

This type of analysis helps reveal how error estimates should be handled for simulations and provides insight to where more information is needed to improve aerodynamic models and estimates. For blunt vehicles of this type, C_{m_q} is typically unstable at very small angles and quickly becomes more stable with increasing angle of attack. For ballistic range tests, the estimated peak value at 0 deg will often have a large uncertainty because for motions where the amplitude is growing rapidly, it is difficult to record multiple

small-amplitude cycles. If the peak value is not accurately captured, the parameter-identification procedures will automatically adjust the width of the peak so that the amplitude growth of small, but not very small, angle motions is captured. Ideally, when including error estimates in simulations, errors in the peak pitch damping should be coupled to errors in the peak width; as the peak value increases, the width of the peak would decrease, and vice versa. Because this would be difficult to implement, adding a delta to the peak that is scaled with the rate at which the pitch damping decreases with σ will overestimate the effect of underpredicting the peak. In the asymptote region, a smaller constant uncertainty can be used.

For the case tested most extensively, $M2$, $M_{\text{nom}} = 0.70$, the estimated values, with errors, for the C_{m_q} parameters are $A1 = -1.553 \pm 0.183$, $A2 = 3.700 \pm 0.83$, and $A3 = -6895$ (fixed). The errors for $A1$ and $A2$ were obtained from the covariance matrices from the least-squares fits of the large- and small-amplitude data, respectively. There were insufficient data to fit $A3$ simultaneously with $A1$ and $A2$, and its estimated value was obtained from parametric studies.

Conclusions

This work presents the estimated nonlinear aerodynamic coefficients, including pitch- and yaw-damping derivatives, for a lifting capsule flying at Mach numbers between 0.70 and 1.25, the range most relevant to parachute deployment for the Orion crew module. The coefficients were derived from aeroballistic range shadowgraph data obtained in the HAFAF at the NASA Ames Research Center. Data and aerodynamic coefficients were also obtained for nonlifting models. Particular focus was given to the pitch-damping characteristics of the capsules.

For angles far away from trim, all five cases tested, lifting models at 3 M numbers and nonlifting models at 2 M numbers, exhibited stability in pitch damping. The lifting cases showed a higher degree of stability than the nonlifting. The two nonlifting cases (nominal Mach numbers 1.10 and 1.25) and the lifting case at approximately Mach 0.70 were significantly unstable in pitch damping at angles close to trim. The drop-off from peak instability as pitch angle moved away from trim was especially rapid for the lifting case. For Mach 0.70 at small sideslip angles, the lifting capsule was also unstable in yaw damping.

Facility calibrations shots using solid steel spheres were included in the investigation, and the authors believe that experimental errors did not substantially contribute to uncertainties in the estimated aerodynamic coefficients. The most significant contributor to uncertainty is the process, during data analysis, of choosing the general mathematical functions with which to model the coefficients. Multistep sensitivity analyses, an example of which, applied to pitch damping for the symmetric model, is given, were used to reduce these uncertainties.

Acknowledgments

The work was supported by the NASA Crew Exploration Vehicle Aerosciences Project, partly through funding to U.S. Government Contract No. NNA04BC25C for Eloret Corporation. The authors gratefully acknowledge the contributions of Don Holt, Don Bowling, Rick Smythe, Chuck Cornelison, Bill Newby, Bob Kruse, Bob Miller, Jorge Rios, Jean–Pierre Wiens, and Shawn Meszaros.

References

[1] Redd, B., Moseley, W. C., and Gamble, J. D., "The Influence of Dynamic Stability Parameters on the Design and Operational Characteristics of the Apollo Launch Abort and Entry Systems," *The Third Technical Workshop on Dynamic Stability Problems*, NASA Ames Research Center, Moffett Field, CA, Nov. 1968.

[2] Moseley, W. C., and Martino, J. C., "Apollo Wind Tunnel Testing Program: Historical Development of General Configurations," NASA TN D-3748, Dec. 1966.

[3] Malcolm, G. N., and Kirk, D. B., "Comparison of Free-Flight and Conventional Wind-Tunnel Stability Tests for Apollo Command Module and Abort Configurations," NASA TM X-1137, Sept. 1965.

[4] Moseley, W. C., Moore, R. H., and Hughes, J. E., "Stability Characteristics of the Apollo Command Module," NASA TN D-3890, March 1967.

[5] Orion Aerodynamic Databook, Ver 0.2," edited by P. Robinson, NASA, Rept. JSC-63402, CXP-72167, Jan. 2007.

[6] Chapman, G. T., and Kirk, D. B., "A Method for Extracting Aerodynamic Coefficients from Free-Flight Data," *AIAA Journal*, Vol. 8, No. 4, 1970, pp. 753–758. doi:10.2514/3.5752

[7] Yates, L. A., "A Comprehensive Automated Aerodynamic Reduction System for Ballistic Ranges," U.S. Air Force Wright Laboratory, Rept. WL-TR-96-7059, Oct. 1996.

[8] Sammonds, R. I., and Dickey, R. R., "Effectiveness of Several Control Arrangements on a Mercury-Type Capsule," NASA TM X-579, Oct. 1961.

[9] Canning, T. N., Seiff, A., and James, C. S., "Ballistic-Range Technology," *AGARDograph*, Vol. 138, Aug. 1970.

[10] Intreiri, P. F., and Kirk, D. B., "High-Speed Aerodynamics of Several Blunt-Cone Configurations," *Journal of Spacecraft and Rockets*, Vol. 24, No. 2, 1987, pp. 127–132. doi:10.2514/3.25885

[11] Yates, L. A., and Venkatapathy, E., "Free-Flight Trim-Angle Predictions for the Aeroassist Flight Experiment," *Journal of Spacecraft and Rockets*, Vol. 29, No. 3, 1992, pp. 335–343. doi:10.2514/3.26356

[12] Brown, J., Yates, L., Bogdanoff, D., Chapman, G. "Free-Flight Testing in Support of the Mars Science Laboratory Aerodynamics Database," *Journal of Spacecraft and Rockets*, Vol. 43, No. 2, 2006, pp. 293–302. doi:10.2514/1.19221

[13] Yates, L., and Chapman, G., "Analysis of Data from Ballistic Range Tests for an Untrimmed CEV Model: Draft Rept.," NASA Task RAA002, Dec. 2006.

[14] Brown, J., Bogdanoff, D., Yates, L., Wilder, M., and Murman, S., "Complex-Trajectory Aerodynamics Data for Code Validation from a New Free-Flight Facility," AIAA, Paper No. 2006-0662, Jan. 2006.

[15] Etkin, B., *Dynamics of Atmospheric Flight*, Wiley, New York, 1972.

[16] Sommer, S. C., and Tobak, M., "Study of the Oscillatory Motion of Manned Vehicles Entering Earth's Atmosphere," NASA 3-2-59A, April 1959.

R. Cummings
Associate Editor